



OPEN ACCESS

EDITED BY

Hu Li,
Southwest Petroleum University, China

REVIEWED BY

Zhe Wang,
China University of Geosciences
Wuhan, China
Wei Ni,
China University of Geosciences
Wuhan, China

*CORRESPONDENCE

Yahao Huang,
hyhtr08916@163.com

SPECIALTY SECTION

This article was submitted to Structural Geology and Tectonics, a section of the journal Frontiers in Earth Science

RECEIVED 02 October 2022

ACCEPTED 08 November 2022

PUBLISHED 12 January 2023

CITATION

Tang Y, Wu Y, Wang R, Huang Y, Xue Y, Chen Z, Xu T, Wang T and Li H (2023), Fluid evolution and paleo-pressure recovery by Raman quantitative analysis in the Shahejie Formation of the western slope belt in Dongpu Sag, Bohai Bay Basin, China. *Front. Earth Sci.* 10:1059909. doi: 10.3389/feart.2022.1059909

COPYRIGHT

© 2023 Tang, Wu, Wang, Huang, Xue, Chen, Xu, Wang and Li. This is an open-access article distributed under the terms of the [Creative Commons Attribution License \(CC BY\)](https://creativecommons.org/licenses/by/4.0/). The use, distribution or reproduction in other forums is permitted, provided the original author(s) and the copyright owner(s) are credited and that the original publication in this journal is cited, in accordance with accepted academic practice. No use, distribution or reproduction is permitted which does not comply with these terms.

Fluid evolution and paleo-pressure recovery by Raman quantitative analysis in the Shahejie Formation of the western slope belt in Dongpu Sag, Bohai Bay Basin, China

Youjun Tang^{1,2}, Yijun Wu¹, Ruyue Wang³, Yahao Huang^{1,2*}, Yifan Xue¹, Zhonghong Chen¹, Tianwu Xu⁴, Ting Wang¹ and Hongbo Li¹

¹Key Laboratory of Exploration Technologies for Oil and Gas Resources (Yangtze University), Ministry of Education, Wuhan, China, ²State Key Laboratory of Oil and Gas Reservoir Geology and Exploitation, Chengdu University of Technology, Chengdu, China, ³SINOPEC Petroleum Exploration and Production Research Institute, Beijing, China, ⁴Exploration and Development Research Institute, Zhongyuan Oilfield Company, SINOPEC, Puyang, China

Inorganic and organic fluids are widely found in sedimentary basins during oil and gas migration and accumulation. This research investigates two types of sandstone reservoirs with different pressure states and fluid evolution of the Shahejie Formation in the western slope belt of Dongpu Sag. Based on petrographic observations, micro-Raman spectroscopy, and fluorescent spectrometry, petroleum inclusions, CH₄-bearing inclusions, and CO₂-bearing inclusions were discovered in quartz-hosted minerals. The pressure–temperature–time–composition (*P–T–t–X*) properties of the CH₄ and CO₂ inclusions were obtained by quantitative Raman analysis and thermodynamic models. Minimum trapped pressure was predicted by the thermodynamic modeling of petroleum inclusions. Saffron yellow petroleum inclusions represent an early Oligocene oil-charging event (~32–30 Ma), and the two kinds of reservoirs were all kept in moderate-overpressure conditions (average pressure coefficient: 1.26). Due to rapid uplift and denudation (Dongying movement) in the middle Oligocene in step II, crude oil degrades into CH₄ and CO₂ (density of CH₄ gas inclusions: 0.1010–0.1339 g/cm³; density of CO₂ gas inclusions: 0.450–0.612 g/cm³) and retains low-maturity (0.67–1.04%) bitumen *in situ*. Tectonic destruction causes the reservoir to be released to normal pressure. With the reburial of the Es₃ Formation, step II entered the middle stage of oil generation again (average pressure coefficient: 0.90). However, in step I, with secondary hydrocarbons occurring, second-stage oil (performance for pale blue fluorescence in petroleum inclusions) accumulated at ~12–0 Ma (late Miocene–Pliocene). The second oil charging event in step I remains a reservoir under high-overpressure conditions (average pressure coefficient: 1.67).

KEYWORDS

quantitative Raman spectroscopy, CH₄ and CO₂, fluid inclusion, Shahejie Formation, Dongpu Sag

Introduction

Reservoir pore fluid plays an important role in petroliferous basins and can reflect the dynamic process of hydrocarbon generation, migration, and accumulation (Dickinson, 1953; Tingay et al., 2009; Guo et al., 2011). Fluid activity (e.g., petroleum, CH₄, and CO₂) in natural strata can be trapped by lattice defects and fracture healing in minerals to form primary or secondary fluid inclusions (Mclimans, 1987; Goldstein, 2001). As independent geochemical systems, geo-fluid parameters such as temperature, pressure, components, and sources contained in fluid inclusions are codes of geological interpretation in relevant geological processes (Haszeldine et al., 1984; Roedder, 1984; Goldstein, 2003). Paleo-fluid pressure recovery and fluid source traces can be used as an index of oil and gas reservoir transformation and adjustment or for research on fault sealing (Gay et al., 2007; Weibull et al., 2010; Li et al., 2010; Wang et al., 2016; Guo et al., 2022). The maintenance of the overpressure state and fluid source are signs of good oil and gas enrichment and preservation conditions (Li et al., 2019; Li et al., 2022; Wang et al., 2016). The most direct and accurate method is to obtain the thermodynamic and physical–chemical data through the entrapment condition of the fluid inclusions (Burruss, 1987; Huang et al., 2018).

Laser Raman microprobe (LRM) spectroscopy, as a new micro-area analysis technique, has the characteristics of high precision and *in situ*, non-destructive and rapid analysis (Zozulya et al., 1998; Osborne and Haszeldine, 1993; Van den Kerkhof and Hein, 2001; Munz et al., 2004). Owing to the Raman quantitative function model, in the wide variation of pressure–temperature, Raman spectroscopy directly determining the total composition and total density of inclusions at abnormal temperatures can be carried out (Seitz et al., 1996; Pironon et al., 2003). Microthermometric measurement and LRM spectroscopy performed for fluid inclusions, combined with thermodynamic modeling, enable fluid inclusion quantitative analysis (e.g., composition, entrapped pressure, and bulk density), representing a key approach to reconstruct *P–T* entrapment conditions (Fabre and Couty, 1986; Gao et al., 2020; Dubessy et al., 1989, 2001; Burke, 2001). Raman spectroscopy can measure CH₄ and CO₂ solubility, salinity, pressure, or density in individual gaseous and aqueous inclusions (peak shift, peak separation, peak area ratio, peak height ratio, etc.) (Dubessy et al., 2001; Azbej et al., 2007; Baumgartner and Bakker, 2009; Caumon et al., 2014; Ou et al., 2015; Zhang et al., 2016; Gao et al., 2017); however, Raman quantitative microanalyses in geological applications are still weak.

The transition of diagenetic fluids in different environments leads to changes in the concentrations of key trace elements and isotopic compositions. The knowledge of alterations of rare earth elements (REEs) (e.g., seawater origin, meteoric water leaching-

percolation, redox reactions, and hydrothermal origin) can be used to identify the extent and characteristics of diagenetic alterations of vein-filling minerals (Munz et al., 2004). These data can then provide information on the migration of geological fluids, stages of vein filling, and variations in diagenetic environments (Saimd and Ali, 2006).

Dongpu Sag is located in the southern Bohai Bay Basin in east China, and the western slope belt of Dongpu Sag is one of the main areas for oil and gas exploration and development in the SINOPEC Zhongyuan Oilfield. Fracture controls the structure-deposition evolution and formation of oil accumulation. Under the microscope work, in addition to oil inclusions, large numbers of primary and secondary gas-bearing fluid inclusions and pore-filled bitumen were found. Raman probe *in situ* analysis revealed that the fluid inclusions contain CH₄ and CO₂ gas. The purpose of this paper is to determine the paleo-fluid composition, paleo-pressure, and fluid charging period in the Shahejie Formation.

Geological setting

Dongpu Sag is located in the southern Bohai Bay Basin, which is part of Linqing Sag (Figure 1). According to the basement morphology and fault features, Dongpu Sag can be divided into five secondary-structural units: western slope belt; western sag belt; central uplift belt; eastern depression belt; and Dong Mingji fault step belt. The sedimentary cover of Dongpu Sag experienced two major stages: Paleogene rift and Neogene depression (Zuo et al., 2017). From old formation to new formation, this was filled with the Paleogene fourth member of the Shahejie Formation (Es₄), the third member of the Shahejie Formation (Es₃), the second member of the Shahejie Formation (Es₂), the first member of the Shahejie Formation (Es₁) and the Dongying Formation (E_d), the Neogene Guantao Formation (N_g), the Minghuazhen Formation (N_m), and the Quaternary. Among them, Es₃ is the basin period of greatest prosperity. It represents the main formation stage of the source rock, salt rock, and favorable reservoir. It can be further divided into the lower (Es₃³), middle (Es₃²), and upper (Es₃¹) sections (Figure 2).

The study area is located in the central part of the western slope belt (Figure 1A). Large faults in the area, such as Changyuan, Shijiaji, Xingzhuang, Wuxingji, and Mazhai, are distributed in the style of goose spread. The slope belt is cut into two east–west fault belts (step I and step II in Figure 1C). Regionally, the Shahejie Formation in the western slope belt of Dongpu Sag mainly develops the source rocks of the first, third, and fourth members of the Paleogene strata, and the lithology is mainly dark mudstone, oil shale, calcareous, dolomitic shale, and calcareous rock. The kerogen type of source rocks is mainly

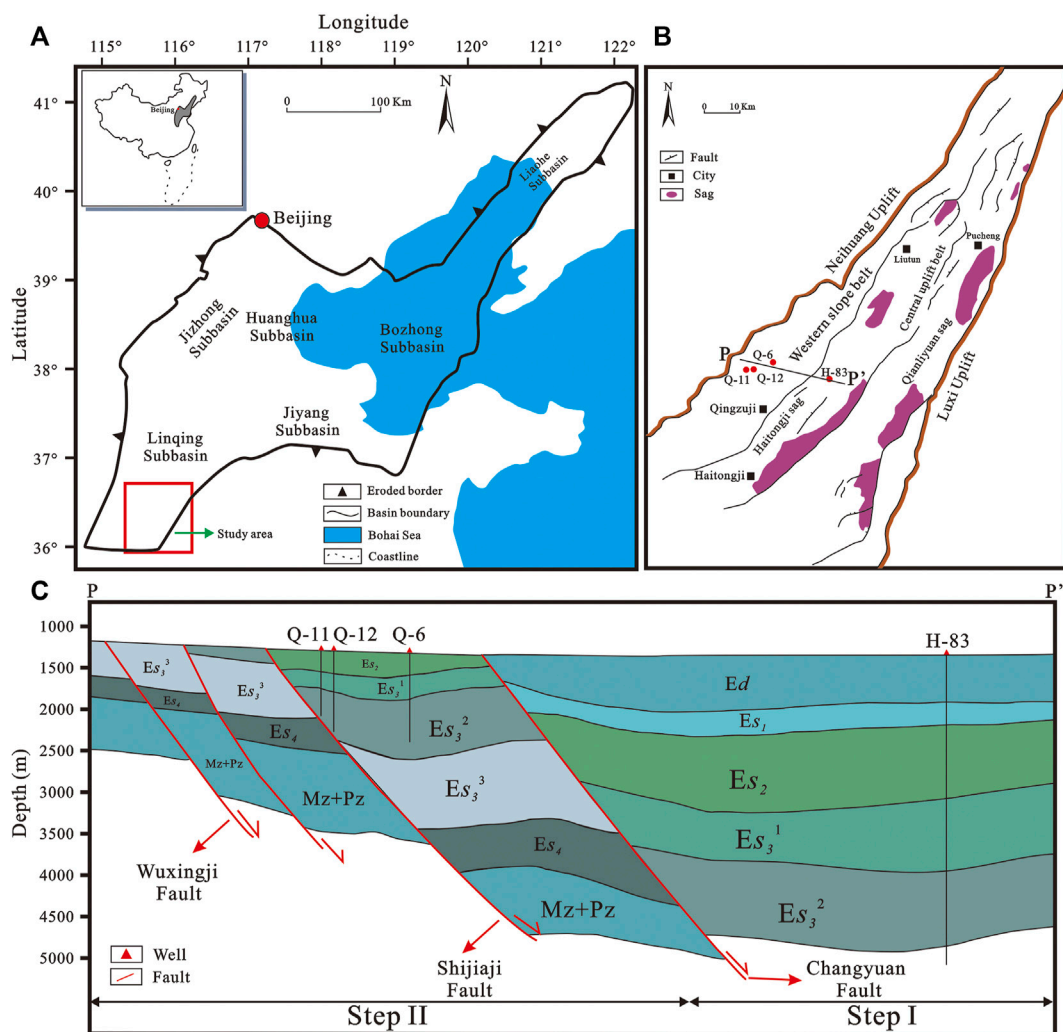


FIGURE 1

(A) Location map of Dongpu Sag in the Bohai Bay Basin. (B) Structural unit division map of Dongpu Sag. (C) Profile p-p' of the present western slope belt. The location of line p-p' is indicated in Figure 1 (adopted from Luo et al., 2016).

mixed, and its parent material mainly comes from lower organisms and some higher plants (Song et al., 2010). The source rocks enter the maturity stage ($R_o=0.5\%$) at a burial depth of approximately 2,500 m, enter the high maturity stage ($R_o=1.3\%$) at a burial depth of approximately 4,000 m, and enter the dry gas stage ($R_o=2.0\%$) at a burial depth of approximately 5,000 m. Source rocks of middle and lower sub-members of Es_3 have also reached the mature hydrocarbon generation stage, which leads to step II having various oil sources, resulting in the wide distribution of oil and gas and enrichment. In the western slope belt, Es_3^3 and Es_3^2 are dominated by the underwater fan, the sedimentary center of the Es_3^3 period is located in the Huzhuangji area, and the filling deposition of the fan middle channel is widely developed, which is mainly composed of gravel medium fine sandstone (Wu and Ye,

2009; Luo et al., 2016). The sedimentary center of the Es_3^2 period moved east to Liutun–Haitongji Sag. At this time, due to the intense activity of the Changyuan and Xingzhuang faults, miniature slump fans often developed in the fault block. The upper member of Es_3 is mainly deltaic deposit, and the development degree of sandstone is relatively poor, mainly distributed channel sand and sheet sand. Structural, lithologic, stratigraphical, and structural–stratigraphical types of traps developed in the study area (Liu et al., 2019).

Sampling and methods

Approximately 30 sandstone core samples were collected from well H-83 in step I and well Q-6, well Q-11, and well Q-12

temperature ($P-T$) entrapment conditions by microthermometry and volumetric analysis using confocal laser scanning microscopy (for details, see [Ping et al., 2013](#); [Pironon and Bourdet, 2008](#)). This reliable method requires T_h and the degree of bubble filling (F_v) as known parameters to determine the C_{7+} molar proportion of petroleum inclusions. The quantitative correlation among the C_{7+} mole fraction and T_{hoil} and F_v can be used to predict the minimum trapped pressure.

Raman spectroscopy

The Raman instrument used was a JY/Horiba LABRAM HR800 (532-nm green laser; 400–500 mW output power) at China University of Geosciences (Wuhan) equipped with 10×/20×/50× long-focus objectives. Peak calibration was used with $\sim 520.7\text{ cm}^{-1}$ polished silicon during the experiments. Components of gaseous fluid inclusions were investigated by setting a 200- μm confocal hole and 300-gr-mm $^{-1}$ grating with a 2,650 cm^{-1} grating center. The accumulative time varied from 0 to 500 s to acquire the optimal signal-to-noise ratio. Options of precise resolution (1,800 gr-mm $^{-1}$ grating and 50- μm aperture) are also necessary for acquiring accurate Raman shifts in terms of single gas phase inclusions. At the same time, neon lamp-corrected measurement should also be applied to acquire strict Raman wavenumbers ([Kawakami et al., 2003](#); [Wang et al., 2011](#); [Dubessy et al., 2012](#); [Huang et al., 2018](#)). The density of pure CH_4 inclusions can be calculated by measuring the Raman shift of the C–H symmetric stretching band (ν_1) of CH_4 ([Seitz et al., 1993, 1996](#); [Lu et al., 2007](#)) at room temperature (25°C, ensured homogenization). After Raman spectrographic collection, the density of pure CH_4 fluid inclusions can be determined by applying different equations (for more details, see [Zhang et al., 2016](#)). The density of pure CO_2 inclusions can be measured as the separation between Fermi diad peaks of CO_2 ([Rosso and Bodnar, 1995](#)). After the acquisition of the Raman spectrum in the homogenized state, the density of CO_2 inclusions is calculated by applying multiple regression formulas (see [Huang et al., 2018](#); [Wang et al., 2019](#)).

NaCl aqueous inclusions bearing dissolved CH_4 are usually coeval with CH_4 -rich fluid inclusions in microfractures or isolated within quartz overgrowths. The quantitative factor ($\text{PAR}/m\text{CH}_4$) of CH_4 - H_2O - NaCl ternary fluids depends on salinity and temperature. To exactly calculate the CH_4 solubility in a NaCl aqueous inclusion at a known temperature, the salinity must be determined first. The salinity of the aqueous fluid inclusions can be determined using the Raman spectra of the $\nu(\text{OH})$ stretching vibration of water (e.g., [Dubessy et al., 1989](#); [Caumon et al., 2015](#)).

I_{3425}/I_{3260} was calculated using the integral Raman intensity ratio of wavenumber intensity at 3,425 cm^{-1} to wavenumber intensity at 3,260 cm^{-1} at 25°C ([Guillaume et al., 2003](#); [Becker et al., 2008](#); [Caumon et al., 2014](#)). The measured I_{3425}/I_{3260} and temperature were substituted into Eq. 1 ($R^2 > 0.997$; [Ou et al., 2015](#)):

$$S = -0.116 IR^2 + 5.805 IR - 6.933 \quad (1)$$

The integration of the Raman peak area ratio (PAR) of the CH_4 ν_1 band ($\sim 2,917\text{ cm}^{-1}$) to the OH stretching band of water in homogenized aqueous inclusions can determine the CH_4 concentration of water-rich fluid inclusions (mol/kg; [Ou et al., 2015](#)):

$$\text{PAR}/m\text{CH}_4 = aT + b \quad (2)$$

where T is the experimental temperature (K) in a homogeneous state. The slope (a) and intercept (b) are determined by the square root of $m\text{NaCl}$ (see [Ou et al., 2015](#)). Based on these parameters and the model of [Duan et al. \(2003\)](#) and [Duan and Mao \(2006\)](#), the density and homogenization pressure (P_h) of water-rich fluid inclusions can be obtained.

The integration of the Raman peak intensity ratio (HR) of the upper band (at $\sim 1,380\text{ cm}^{-1}$) of the CO_2 Fermi dyad to the OH stretching band of water placed into the formula mentioned previously permits calculation of the concentration of CO_2 in water (mol/kg; [Guo et al., 2014](#)):

$$\frac{\text{HR}}{m\text{CO}_2} = a \times T + b, \text{ at } T > 404.45. \\ a = -2.39 \times 10^{-4}, b = 0.202. \quad (3)$$

With these parameters, the density of water-rich fluid inclusions can be obtained based on [Duan and Sun \(2003\)](#).

Raman spectroscopy calculation of organic maturity

Thermal maturity can be estimated through multilinear regression analysis of Raman spectroscopic parameters of carbonaceous material ([Wilkins et al., 2014, 2015, 2018](#)). The peak separation distance, peak height ratio, and full width at half maximum (FWHM) of the G (1250–1450 cm^{-1}) and D (1500–1605 cm^{-1}) bands can be used to calculate the equivalent vitrinite reflectance (EqVR%). The application details of the equations are described by [Liu et al. \(2013\)](#).

Basin modeling

BasinMod-1D (Version 7.06) software was adopted for the simulation of burial and thermal histories, which integrates the lithology, stratigraphic thickness, erosion

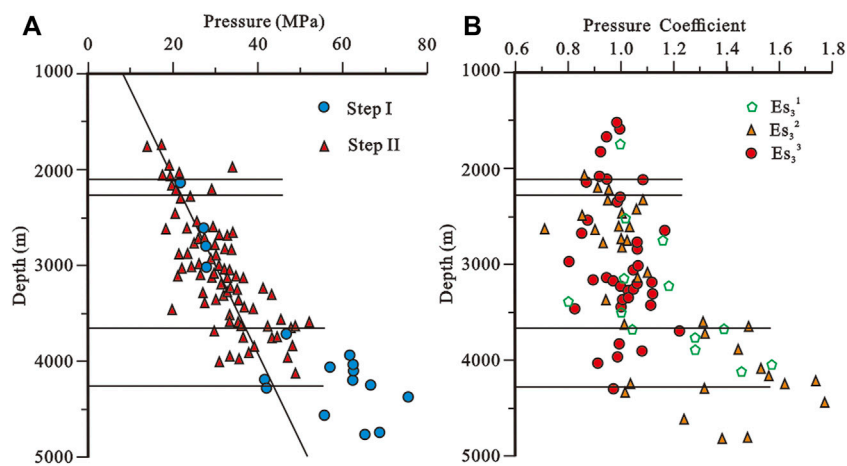


FIGURE 3 (A) Statistics of measured formation pressure and depth at different structural steps in the western slope belt of Dongpu Sag. (B) Statistics of the current pressure coefficient and depth at different horizons in the western slope belt of Dongpu Sag.

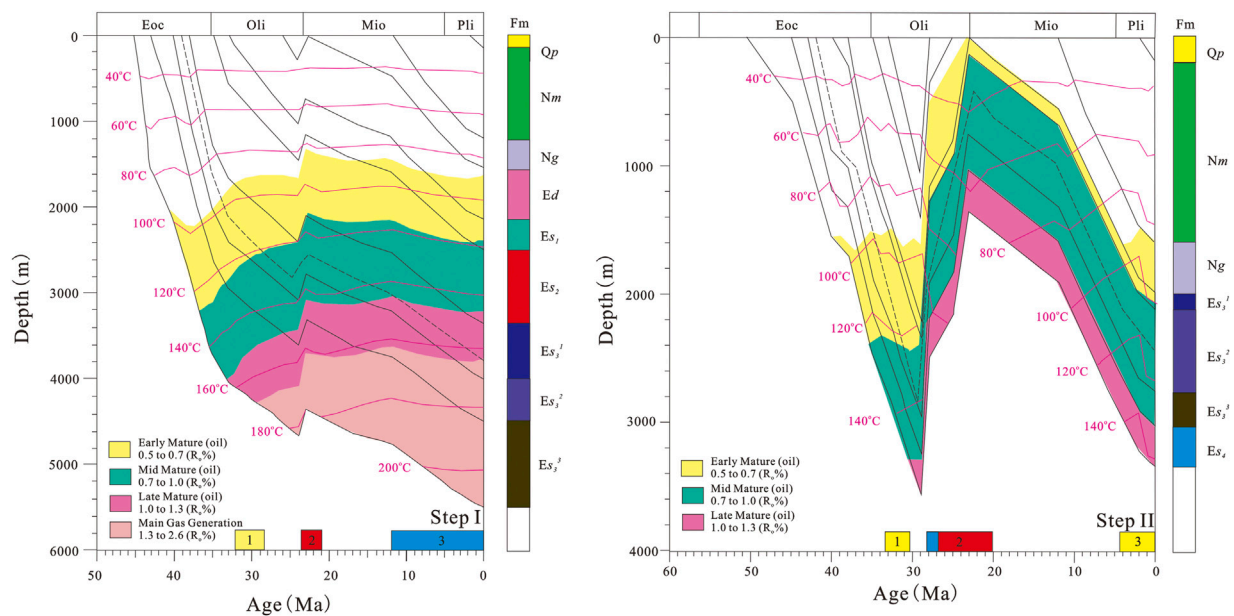
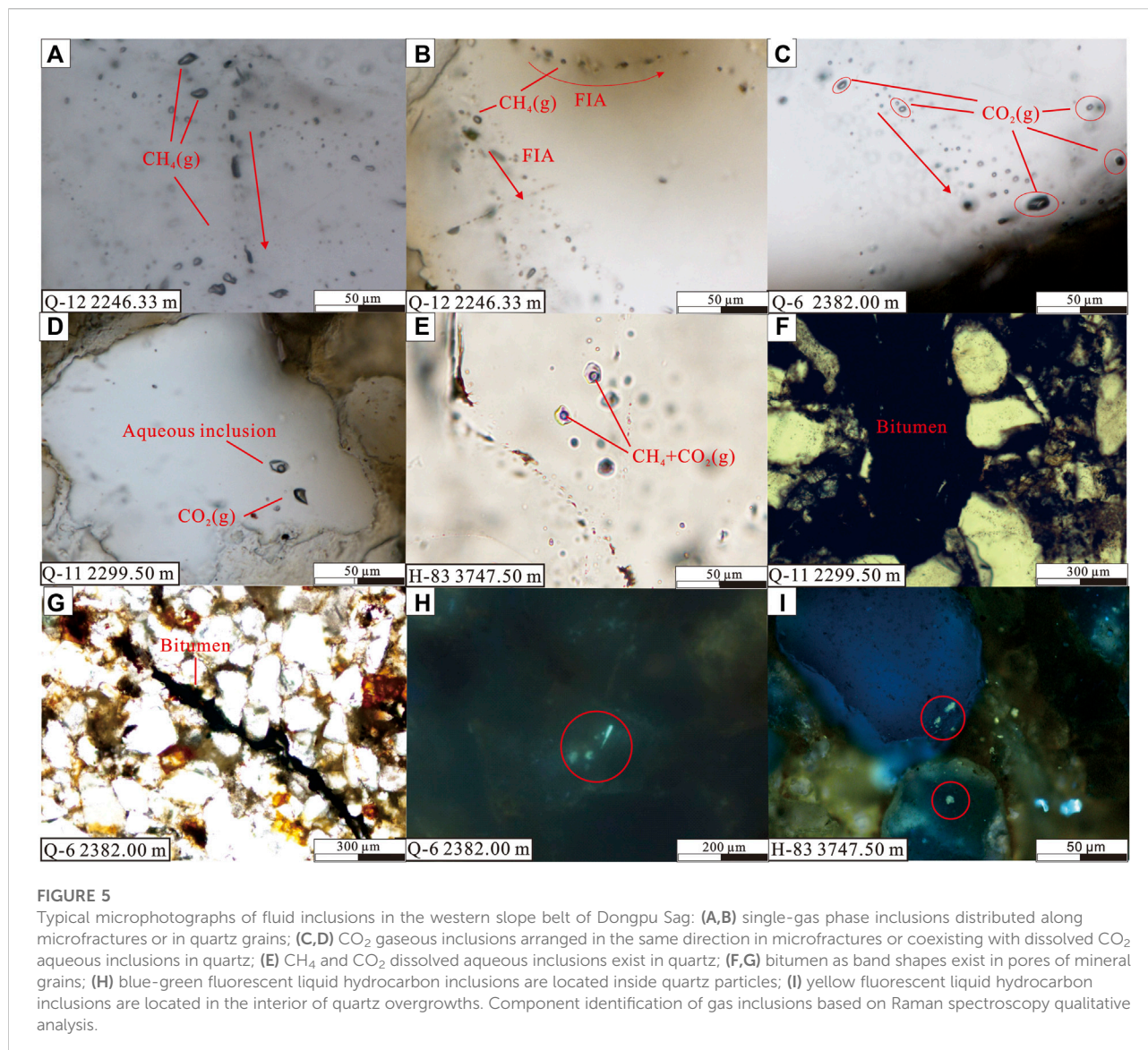


FIGURE 4 Paleocene Formation burial histories of steps I and II, illustrating the CH₄ and CO₂ charging times and multiple-staged oil charging times. The yellow frame represents the trapped period of yellow petroleum inclusions, the red frame represents the trapped period of CH₄ and CO₂, and the blue frame represents the trapped period of blue petroleum inclusions.

thickness, absolute age, vitrinite reflectance, and measured borehole temperature data. Well completion reports (e.g., DST data) from the SINOPEC Zhongyuan Oilfield provide the measured R_o and borehole temperature values (Figure 3).

Thermal history simulation was mainly corrected using the vitrinite reflectance and temperature. The simulation results of the burial history of well Q-12 in step II and well H-83 in step I are shown in Figure 4.



Results

Reservoir pressure characteristics

Analysis of oil testing pressure data shows that the reservoir pressure of different structural units in the study area has different development characteristics (Figure 3). The measured burial depth of the formation pressure point between 1,100 and 4,900 m ranges from 14.0 to 76.0 MPa, the pressure coefficient is 0.77–1.80, and the formation pressure increases with the burial depth. Es₁, Es₂, Es₃, and Es₄ were dominated by normal pressure. The shallow strata (<3,400 m) of Es₃¹ and Es₃² are mainly normal pressure, but the deep part is mostly in overpressure conditions. Overpressures

are widespread in step I, but step II mainly occurs under normal pressure conditions, and faults in the distribution of the reservoir pressure have a significant control effect.

Fluid inclusion classification

CH₄, H₂O, CO₂, and petroleum fluids can be trapped by quartz grains or overgrowths during diagenetic processes. Petrographic observations at room temperature and the identification of UV fluorescence and Raman characteristic peaks can be comprehensively used to precisely classify the fluid inclusion assemblages (FIAs) into five types (Figures 5, 6):

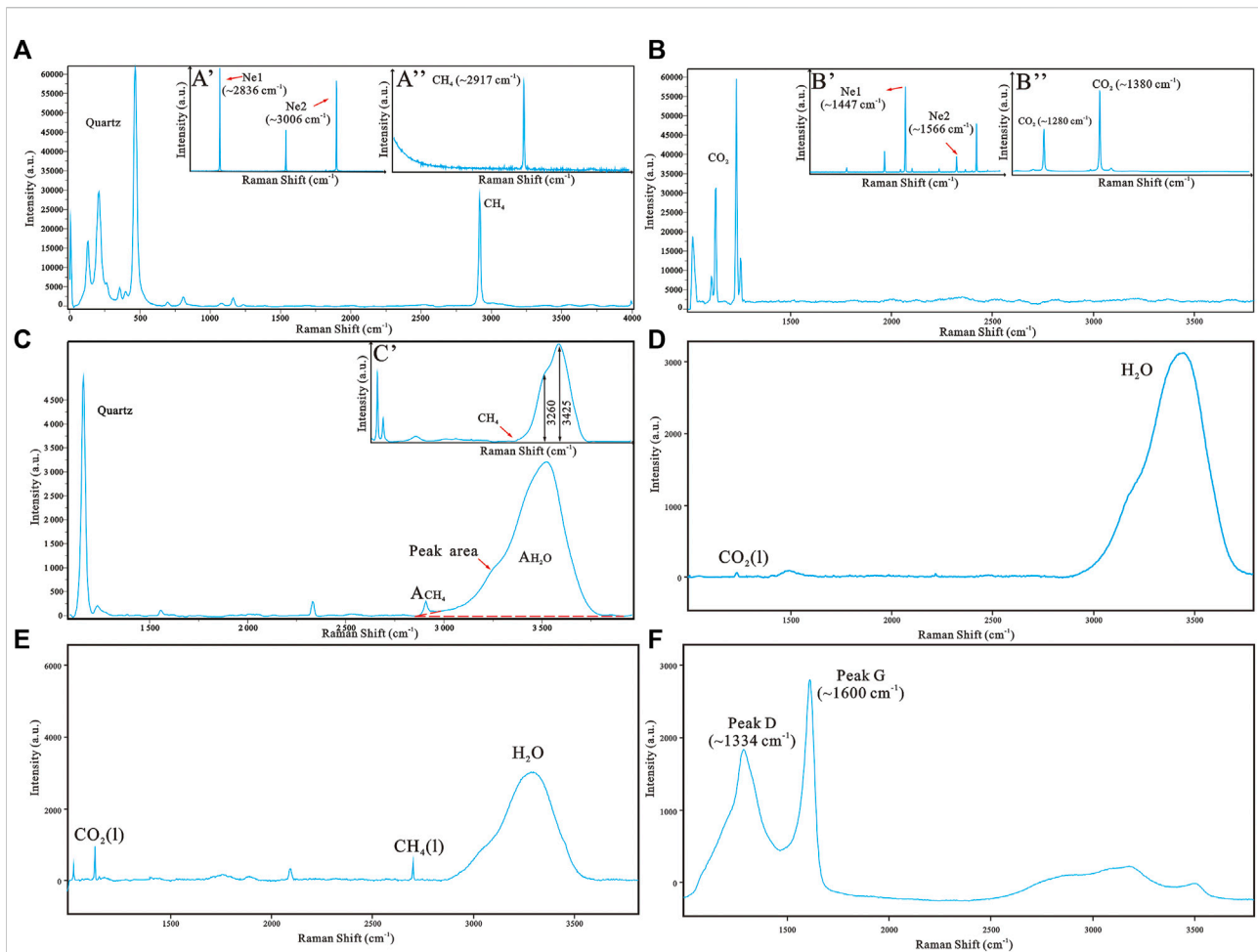


FIGURE 6

Classical Raman spectra of CH_4 - and CO_2 -bearing fluid inclusions: (A) spectra of the pure CH_4 component collected using the 300 gr.mm^{-1} grating in quartz [the CH_4 symmetric stretching band (ν_1) peak was collected using the $1,800 \text{ gr.mm}^{-1}$ grating with a Ne lamp]; (B) spectra of the pure CO_2 component collected using the 300 gr.mm^{-1} grating in quartz [the CO_2 Fermi double peak was collected using the $1,800 \text{ gr.mm}^{-1}$ grating with a Ne lamp]; (C) spectra of CH_4 - H_2O - NaCl components collected using the 300 gr.mm^{-1} grating obtained in the homogeneous state [(C') is the spectra of the liquid part at room temperature]; (D) spectra of CO_2 - H_2O - NaCl components collected using the 300 gr.mm^{-1} grating obtained in the homogeneous state; (E) spectra of CH_4 - CO_2 - H_2O - NaCl components collected using the 300 gr.mm^{-1} grating obtained in the homogeneous state; (F) G ($\sim 1334 \text{ cm}^{-1}$) and D ($\sim 1600 \text{ cm}^{-1}$) peaks of bitumen were collected at room temperature.

Inclusion type I

These single-vapor (VCH_4) inclusions are most abundant in microfractures or occur in the overgrowths and are usually coeval with dissolved CH_4 aqueous inclusions (Figures 5A,B), representing secondary generation. The diameters vary from 8 to $15 \mu\text{m}$ with rectangular or irregular shapes.

Inclusion type II

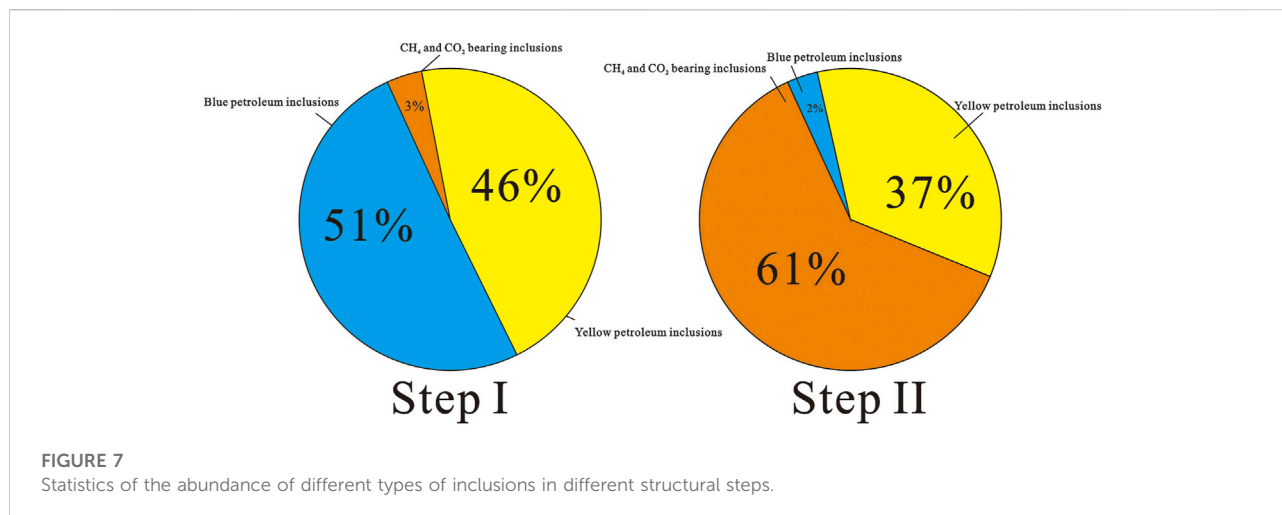
This type of inclusion is one-phase CO_2 gas inclusions coexisting with CO_2 -dissolved aqueous inclusions found along healed microfractures and quartz overgrowths (Figures 5C,D), implying a secondary origin. The diameters range from 10 to $17 \mu\text{m}$. The sizes and shapes of primary and secondary inclusions do not significantly differ.

Inclusion type III

With the spectral collection of homogeneous inclusions, dissolved CO_2 and CH_4 aqueous inclusions are found in quartz grains. They generally have elliptical to circular shapes (Figure 5E). The diameters range from 10 to $17 \mu\text{m}$.

Inclusion type IV

These inclusions are two-phase (L and V) petroleum inclusions. The characteristics of QF_{535} and λ_{max} show saffron yellow and pale blue fluorescence. They are distributed along microfractures or occur in clusters (Figures 5H,I), implying primary and secondary origins. The diameters range from 7 to $15 \mu\text{m}$. These HC inclusions are irregular, elliptical, and rod-shaped.



The abundance statistics of different component types of fluid inclusions have indicative significance for the fluid activity characteristics of reservoirs (Figure 7). The low abundance of CH₄ and CO₂ gas inclusions accounts for only 3% in well H-83 of step I. Blue and yellow fluorescent inclusions accounted for 51% and 46%, respectively. The abundance of blue fluorescent inclusions in each well in step II was low (2%), while that of CH₄ and CO₂ gas was high (61%), and that of yellow fluorescent oil accounted for 37%.

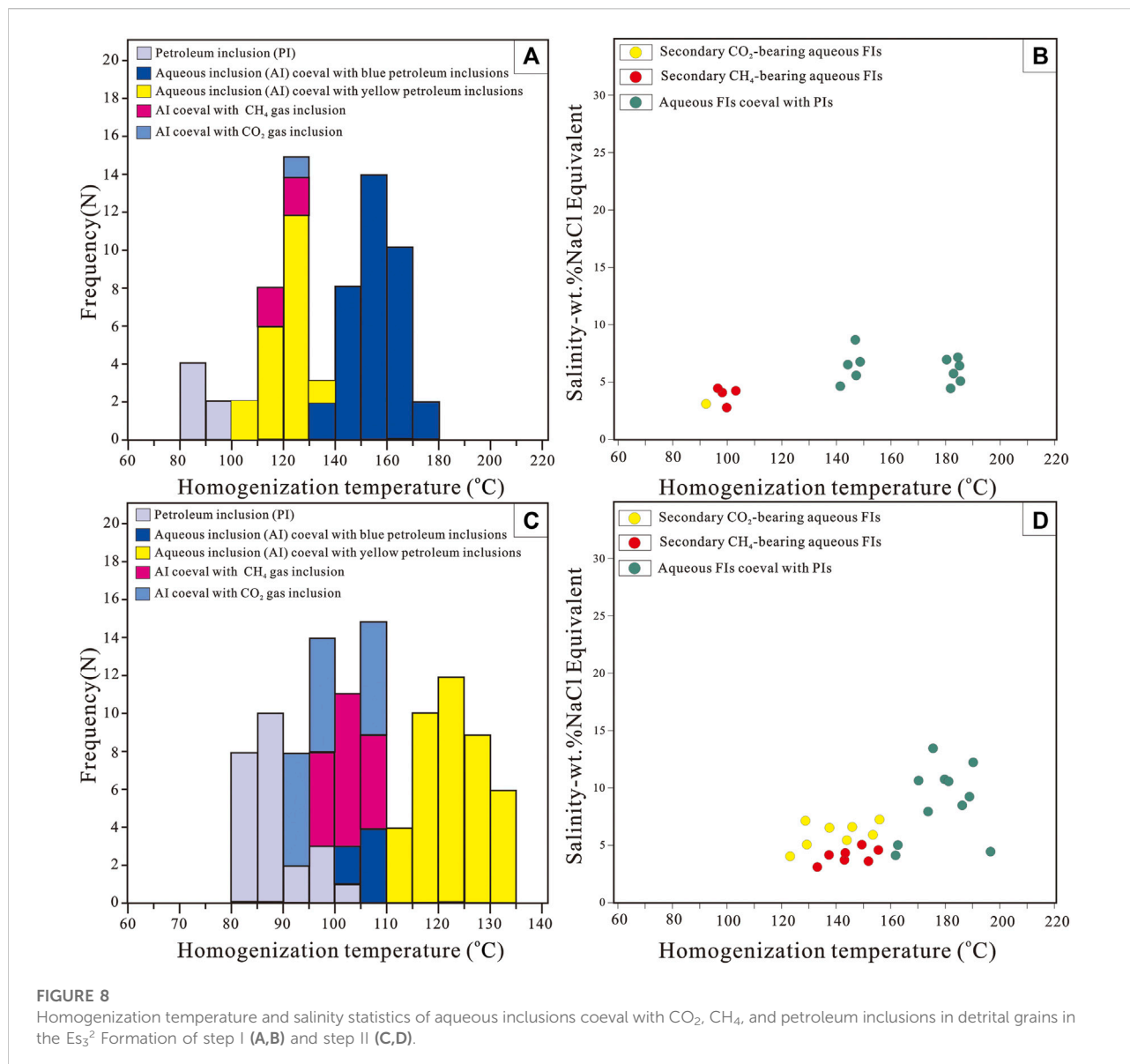
Microthermometry

Aqueous fluid inclusions coeval with CH₄ and CO₂ inclusions in quartz were selected for salinity measurements by the method of height ratio (I_{3425}/I_{3260}) calculation of the water band. Secondary aqueous fluid inclusions coeval with petroleum inclusions were heated to a homogeneous state by the disappearance of the vapor bubble. The salinities (wt% NaCl equivalent) of these fluid inclusions were calculated based on their final ice-melting temperatures ($T_{m, ice}$; Bodnar, 1993). Figures 8A–D show the statistical distribution of salinity and homogenization temperature of different types of inclusions in each well located in step I and Step II, respectively. The homogenization temperature and salinity of reservoir inclusions in step I have the following characteristics. The homogenization temperatures of aqueous inclusions, which are coeval with CO₂ and CH₄ gas inclusions, range from 110 to 130°C (Figure 8A). The salinity interval of these water-rich inclusions varies between 2.7 and 4.9 wt% NaCl (Figure 8B). The bimodal T_h distribution of aqueous inclusions coeval with yellow petroleum inclusions is 110–130°C, and that coeval with blue petroleum inclusions is 150–160°C. The $T_{m, ice}$ of these water-rich inclusions varies between –2.6 and –5.2°C, with a salinity interval of

4.7–8.1 wt% NaCl. In wells Q-6, Q-11, and Q-12, the homogenization temperatures of aqueous inclusions, which are coeval with CH₄ gas inclusions, range from 95 to 110°C (Figure 8C). The salinity interval of these water-rich inclusions varies between 3.5 and 5.3 wt% NaCl. The homogenization temperatures of aqueous inclusions, which are coeval with CO₂ gas inclusions, range from 90 to 100°C and 105 to 110°C. The salinity interval is 3.4–7.3 wt% NaCl. The bimodal T_h distribution of aqueous inclusions coeval with yellow petroleum inclusions is 115–130°C, and that coeval with blue petroleum inclusions is 100–110°C. The $T_{m, ice}$ of these water-rich inclusions varies between –2.3 and –9.8°C, with salinity intervals of 3.9–13.7 wt% (Figure 8D).

Quantitative Raman analysis of fluid inclusions

The pressure and density of secondary CH₄ gas fluid inclusions in quartz can be measured using quantitative Raman analysis. Figures 6A,C exhibit the typical Raman spectrum of CH₄-system fluid inclusions, which were classified based on the petrographic characteristics and compositions in a homogeneous state. Table 1 lists the data for 15 pure CH₄ inclusions (in type I), including their densities, obtained from the C–H symmetric stretching band (ν_1) of methane (Figure 6A, A' and A''). The density varies from 0.1772 to 0.1785 g/cm³ in the wells of step I (average value: 0.1779 g/cm³). The density varies from 0.1010 to 0.1339 g/cm³ in the wells of step II (average value: 0.1126 g/cm³). The homogenization pressure (P_h) is calculated using the thermodynamic model (Peng and Robinson, 1960) with consideration of the densities and T_h of coeval aqueous inclusions. P_h varies from 38.00 to 38.06 MPa (average value: 38.03 MPa) in step I and from 18.29 to 25.50 MPa (average value:



20.90 MPa) in step II. Meanwhile, with the discovery of CO₂-bearing inclusions (Figure 6B), 13 pure CO₂ inclusions (in type II) were quantified and are shown in Table 2. The density varies from 0.608 to 0.662 g/cm³ (average value: 0.555 g/cm³) in step I and from 0.450 to 0.612 g/cm³ (average value: 0.555 g/cm³) in step II. P_h varies from 32.82 to 39.56 MPa (average value: 36.19 MPa) in step I and from 19.34 to 28.68 MPa (average value: 24.94 MPa) in step II.

Tables 3, 4 show the data compilation of four dissolved CH₄ inclusions in NaCl aqueous inclusions (in type I) and three dissolved CO₂ inclusions in NaCl aqueous inclusions (in type I), which were analyzed by Raman spectroscopy in a homogeneous state (Figures 6C,D). The methane content (mCH_4) of the dissolved methane inclusions can be

determined and ranges from 0.387 to 0.690 mol/kg. The CO₂ content (mCO_2) of the dissolved CO₂ inclusions can be mainly determined and ranges from 0.223 to 0.335 mol/kg.

Raman spectral calculation of bitumen maturity

The Raman maturity method can achieve targeted and convenient determination (e.g., organic matter in reservoir sandstone). A large amount of residual bitumen was found in the Paleocene reservoirs of the western slope belt in Dongpu Sag (Figures 5F,G). Residual bitumen is usually observed in the grain pores of quartz. The Raman peak parameters of bitumen were

TABLE 1 Summary of Raman quantitative analysis of pure CH₄ inclusions.

No.	Well	Depth (m)	ν_{true} (cm ⁻¹)	Density (g/cm ³) ^a	Coeval aqueous inclusions homogenization temperature (°C)	Reconstructed trapped pressure (MPa) ^b	Pressure coefficient
1	Q-12	2299.5	2914.75	0.1046	101.5	18.98	0.90
2	Q-12	2299.5	2914.72	0.1058	103.1	19.31	0.92
3	Q-12	2299.5	2914.68	0.1073	103.1	19.59	0.93
4	Q-12	2246.3	2914.49	0.1149	107.8	21.47	1.01
5	Q-12	2246.3	2914.36	0.1201	106.0	22.36	1.05
6	Q-11	2398.4	2913.55	0.1331	108.8	25.21	1.18
7	Q-11	2398.4	2913.58	0.1339	108.8	25.50	1.20
8	Q-11	2398.4	2913.55	0.1314	108.8	25.00	1.17
9	Q-11	2591.7	2914.84	0.1010	107.5	18.72	0.88
10	Q-6	2595.5	2914.72	0.1058	111.7	19.97	0.91
11	Q-6	2588.0	2914.81	0.1022	98.6	18.29	0.91
12	Q-6	2588.0	2914.82	0.1018	104.8	18.67	0.89
13	Q-6	2588.0	2914.84	0.1019	104.8	18.69	0.90
14	H-83	3747.50	2912.35	0.1785	120.8	38.00	1.45
15	H-83	3747.50	2912.38	0.1772	123.5	38.06	1.42

^a: Density calculated following Zhang et al. (2016).

^b: Homogenization pressure calculated following Peng and Robinson (1960).

TABLE 2 Summary of Raman quantitative analysis of pure CO₂ inclusions.

No.	Well	Depth (m)	Distance of fermi doublet (cm ⁻¹)	Density (g/cm ³) ^a	Coeval saline inclusion homogenization temperature (°C)	Reconstructed trapped pressure (MPa) ^b	Pressure coefficient
1	Q-12	2246.3	103.31	0.450	98.5	19.34	0.88
2	Q-12	2246.3	103.54	0.540	98.5	23.36	1.06
3	Q-12	2246.3	103.43	0.496	98.5	21.28	0.97
4	Q-12	2299.5	103.65	0.586	100.8	26.44	1.20
5	Q-12	2299.5	103.56	0.548	100.8	24.32	1.11
6	Q-11	2398.4	103.58	0.557	100.8	24.76	1.13
7	Q-11	2398.4	103.65	0.586	100.8	26.44	1.20
8	Q-6	2588.0	103.63	0.578	101.0	25.99	1.18
9	Q-6	2588.0	103.62	0.573	105.7	26.92	1.22
10	Q-6	2595.5	103.63	0.578	104.3	26.82	1.22
11	Q-6	2595.5	103.71	0.612	103.1	28.68	1.30
12	H-83	3747.50	103.70	0.608	119.4	32.82	1.23
13	H-83	3747.50	103.83	0.665	125.3	39.56	1.50

^a: Density calculated following Huang et al. (2018).

^b: Homogenization pressure calculated following Peng and Robinson (1960).

obtained by *in situ* Raman observation and software calculation, and equivalent vitrinite reflectance (EqVR%) was calculated (Table 5). In the Es₃² Formation of wells Q-12, Q-11, and Q-6, the separation of

the G and D peaks can be used to calculate the maturity of bitumen (Figure 6F). The EqVR% of these residual bitumen ranges between 0.67% and 1.04%. They are characterized by low maturity.

TABLE 3 Dissolved CH₄ in NaCl aqueous inclusions obtained by Raman quantitative analysis.

No.	Well	Depth (m)	PAR (CH ₄ /H ₂ O)	IR (I3425 cm ⁻¹ /I3260 cm ⁻¹) ^a	Salinity (mol.kg ⁻¹) ^b	Homogenization temperature (°C)	mCH ₄ (mol.kg ⁻¹) ^c
1	Q-12	2299.5	0.015335	1.44435	1.21	108.8	0.690
2	Q-12	2299.5	0.013145	1.47508	1.38	107.5	0.595
3	Q-12	2246.3	0.008459	1.52394	1.64	99.3	0.387
4	Q-11	2398.4	0.009840	1.48286	1.42	95.6	0.446

^a: IR: peak intensity ratio, calculated by collecting spectra at 25 °C.

^b: Salinity calculated following [Ou et al. \(2015\)](#).

^c: mCH₄ calculated following [Ou et al. \(2015\)](#).

TABLE 4 Dissolved CO₂ in NaCl aqueous inclusions obtained by Raman quantitative analysis.

No.	Well	Depth (m)	HR (CO ₂ /H ₂ O)	IR (I3425 cm ⁻¹ /I3260 cm ⁻¹) ^a	Salinity (mol.kg ⁻¹) ^b	Homogenization temperature (°C)	mCO ₂ (mol.kg ⁻¹) ^c
1	Q-12	2299.5	0.022	1.66	2.38	98.1	0.223
2	Q-12	2299.5	0.025	1.47	1.35	100.8	0.254
3	Q-6	2595.5	0.033	1.53	1.68	103.1	0.335

^a: IR: peak intensity ratio, calculated by collecting spectra at 25 °C.

^b: Salinity calculated following [Ou et al. \(2015\)](#).

^c: mCH₄ calculated following [Guo et al. \(2014\)](#).

TABLE 5 Raman spectral parameters of vitrinite from Dongpu Sag samples.

No.	Well	Depth (m)	$\nu\text{G}-\nu\text{D}$ cm ⁻¹	HG/HD cm ⁻¹	RaMM EqVR% ^a
1	Q-12	2246.3	221.17	0.924	0.67
2	Q-12	2246.3	221.91	0.916	0.71
3	Q-12	2246.3	227.48	0.922	1.01
4	Q-12	2299.5	227.78	0.932	1.02
5	Q-12	2299.5	226.82	0.934	0.97
6	Q-11	2398.4	225.22	0.939	0.88
7	Q-11	2398.4	226.91	0.963	0.98
8	Q-11	2591.7	228.17	0.757	1.04
9	Q-11	2591.7	225.33	0.949	0.89
10	Q-11	2591.7	227.90	0.990	1.03
11	Q-6	2588.0	227.16	0.947	0.99
12	Q-6	2588.0	223.60	1.056	0.80
13	Q-6	2595.5	225.91	0.970	0.92
14	Q-6	2595.5	225.43	0.913	0.90

$\nu\text{G}-\nu\text{D}$: separation of the positions of the G and D bands. H: height of peak. RaMM: Raman maturity. Method. EqVR%: equivalent vitrinite reflectance.

^a: Equations following [Liu et al. \(2013\)](#).

Minimum trapped pressure of petroleum inclusions

According to parameters, such as homogenization temperature, petroleum inclusion composition, and bubble filling degree of oil inclusions and coexisting

aqueous inclusions, the minimum trapped pressure (P_t) of inclusions can be obtained by PVTsim software simulation and fluorescence spectra ([Figure 9](#)).

The content of CH₄ (C₁) in petroleum inclusions of the E₈³ Formation in wells Q-6, Q-11, and Q-12 ranges from 14.92% to 30.82%, and the content of C₇₊ (hydrocarbons

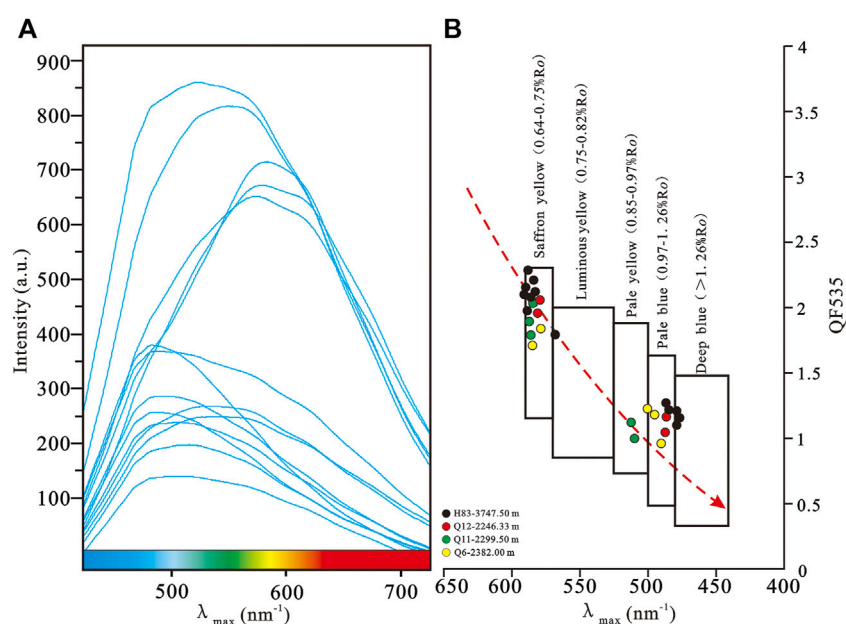


FIGURE 9 Microfluorescence spectra of liquid hydrocarbon inclusions (A) and λ_{max} (wavelength of the maximum intensity) versus QF_{535} (ratio of the 535–750 nm flux to the 430–535 flux) diagram (B).

with carbon numbers over 7) varies from 43.33% to 61.08%. The oil content of petroleum inclusions varies from 80.5 to 95.7°C. The minimum trapped pressures of yellow and blue petroleum inclusions range from 19.08 to 27.87 MPa. The content of C_1 in the petroleum inclusions of the Es_3^2 Formation in the H-83 well ranges from 25.88% to 52.01%, and the content of C_{7+} varies from 19.98% to 48.60%. The oil content of petroleum inclusions varies from 80.5 to 88.7°C. The minimum trapped pressure of blue petroleum inclusions ranges from 42.91 to 54.46 MPa, and the minimum trapped pressure of yellow petroleum inclusions ranges from 32.76 to 34.45 MPa (Table 6).

Discussion

Fluid evolution sequence in the western slope belt

From the microscopic observation of the Es_3^2 Formation in the sandstone reservoir sample, three kinds of fluid activities (petroleum, CH_4 , and CO_2) are identified. Microthermometry was used to measure the homogenization temperature of aqueous inclusions, which was related to different types of fluid inclusions (petroleum, CH_4 , and CO_2). The T_h throwing-dot method can be used to estimate the CH_4 , CO_2 and oil accumulation times (Figure 4) (Haszeldine et al., 1984; Horsfield and McLimans,

1984). Burial histories show the reservoir in two different steps undergoing different fluid evolution processes. In well H-83 of step I, saffron yellow petroleum inclusions with maturation ranges of 0.64–0.75% R_o accumulated at ~32–29 Ma (T_h interval: 110.0–130.0°C; yellow frame in Figure 4). CH_4 and CO_2 fluid accumulated at ~24–21 Ma (T_h interval: 120–130.0°C; red frame in Figure 4). Late generated oil (pale blue petroleum inclusions) with high maturation in 0.97–1.26% R_o accumulated at ~12–0 Ma (T_h interval: 150.0–160.0°C; blue frame in Figure 4). In wells Q-6, Q-11, and Q-12 of step II, saffron yellow petroleum inclusions accumulated at ~33–30 Ma, and after the uplift and denudation of the Dongying movement, the source rocks were buried deep again. Secondary oil generation accumulated at 4–0 Ma (T_h interval: 115.0–125.0°C; yellow frame in Figure 4). Low-abundance pale blue petroleum inclusions and high-abundance CH_4 and CO_2 gas inclusions are observed, which accumulated at ~28–20 Ma (T_h interval: 95.0–110.0°C; red and blue frame in Figure 4).

Degradation and oxidation of crude oil

Currently, all development wells in step I and step II produce oil and no natural gas. In each well of step II, except for the discovery of multistage petroleum fluids, the greatest significance is that a large abundance of CH_4 and CO_2 -gas-bearing inclusions is detected *in situ* by LRM spectroscopy. At the same time, a large amount of bitumen fills the grain pores of the sandstone

TABLE 6 Petroleum inclusion trapped pressure analysis summary.

No.	Well	Depth (m)	T_{hoil}	T_{haq} (°C)	Fv (%)	C ₁ (mol%)	C ₇₊ (mol%)	Fluorescence color	Reconstructed trapped pressure (MPa) ^a	Pressure coefficient
1	Q-12	2299.5	89.5	120.8	5	24.36	50.19	Yellow	27.86	1.26
2	Q-12	2299.5	90.1	125.4	4	15.48	59.78	Yellow	26.84	1.22
3	Q-12	2299.5	91.6	115.4	6	29.43	44.83	Blue	26.11	1.19
4	Q-12	2299.5	83.1	101.3	4	20.05	54.73	Yellow	19.08	0.87
5	Q-12	2299.5	80.5	103.1	4	21.73	52.96	Yellow	22.28	1.01
6	Q-11	2398.4	88.6	114.5	6	30.82	43.33	Yellow	27.87	1.23
7	Q-11	2398.4	91.5	115.6	6	29.48	44.78	Blue	26.29	1.20
8	Q-11	2591.7	95.7	120.9	6	27.43	46.96	Yellow	25.84	1.04
9	Q-6	2595.5	91.5	123.4	5	23.21	51.40	Yellow	27.64	1.24
10	Q-6	2588.0	90.5	118.6	4	15.22	60.09	Yellow	22.69	1.03
11	Q-6	2588.0	91.8	120.6	4	14.38	61.08	Yellow	22.74	1.01
12	H-83	3747.50	83.6	120.2	16	52.01	19.98	Blue	44.66	1.78
13	H-83	3747.50	88.7	124.3	15	49.84	21.87	Blue	42.91	1.71
14	H-83	3747.50	87.7	146.7	16	51.19	20.67	Blue	54.46	1.60
15	H-83	3747.50	86.6	136.6	14	49.06	22.61	Blue	49.16	1.82
16	H-83	3747.50	86.3	153.8	7	35.85	37.66	Blue	51.48	1.42
17	H-83	3747.50	80.5	113.6	6	34.23	39.52	Yellow	33.38	1.29
18	H-83	3747.50	81.0	120.4	5	28.95	45.35	Yellow	34.45	1.31
19	H-83	3747.50	86.8	125.1	5	25.88	48.60	Yellow	32.76	1.26

^a: Reconstructed trapped pressure calculated following Ping et al. (2013).

reservoir. The EqVR% of bitumen ranges from 0.67% to 1.04%. According to the vitrinite reflectivity and occurrence, it belongs to the degraded and oxidized bitumen formed *in situ*. The coexistence of CH₄ and CO₂ gas in fluid inclusions indicates that the early oil in the reservoir underwent degradation and oxidation. Crude oil with a high carbon number will produce many light components (mainly methane) and CO₂ after degradation and leave low-maturity bitumen *in situ* (Revesz et al., 1995; Head et al., 2010). The CH₄ and CO₂ fluid trapping period occurred after the first stage of the oil charging event. At this time, step II of the western slope belt experienced a strong uplifting structure and erosion because of the Dongying movement. Strong tectonic movement over a short period of time causes the opening of the fault and the exposure of crude oil. The Dongying movement has different tectonic control functions for different fault blocks. Compared with step II, step I has a very weak tectonic uplift and denudation, and the differences in the abundance of CH₄ and CO₂ gas inclusions in the two regions are also indicative (Figure 7).

Palaeo-pressure characteristics

Aqueous inclusions are simultaneously observed alongside gas/petroleum inclusions, indicating that immiscible FIAs were trapped

during mineral crystallization (Roedder, 1984; Goldstein, 1986; Diamond, 2001; Hurai, 2010). Isochore calculations of fluid trapped pressure follow the approach of a two-phase immiscible field (Pironon, 1990; Thiery et al., 2000; Gao et al., 2017). Based on the combination of the Raman spectra with the relevant thermodynamic model (Peng and Robinson, 1960; Duan and Mao, 2006), the component concentration and density of the water-rich and gas-rich phases can be obtained (Dubessy et al., 2001; Becker et al., 2008; Lecumberri-Sanchez et al., 2012; Mao et al., 2013).

In petroliferous sedimentary basins, reservoir pore fluids usually consist of oil, gas, and formation water. Pore fluid pressure is one of the key parameters for reservoir fluid evaluation. The parameters of the formation fluid pressure and pressure coefficient are usually used in pore pressure characterization. The formation fluid pressure coefficient (P_c) here refers to the ratio of the actual formation fluid pressure (P_f) to the hydrostatic pressure (P_{hyd}) at the same depth. It is a main parameter used to identify abnormal formation pressure (Law and Spencer, 1998). In this study, measured formation pressure and temperature data sets from drill stem tests (DSTs) were supplied by the SINOPEC Zhongyuan Oilfield (Figure 3). The current measured pressure coefficient of the Es₃² Formation ranges from 1.50 to 1.66 (high overpressure) in step I and from 0.95 to 1.02 (normal pressure) in step II (Table 6). The trapped pressure of fluid inclusions represents the pore fluid pressure in the

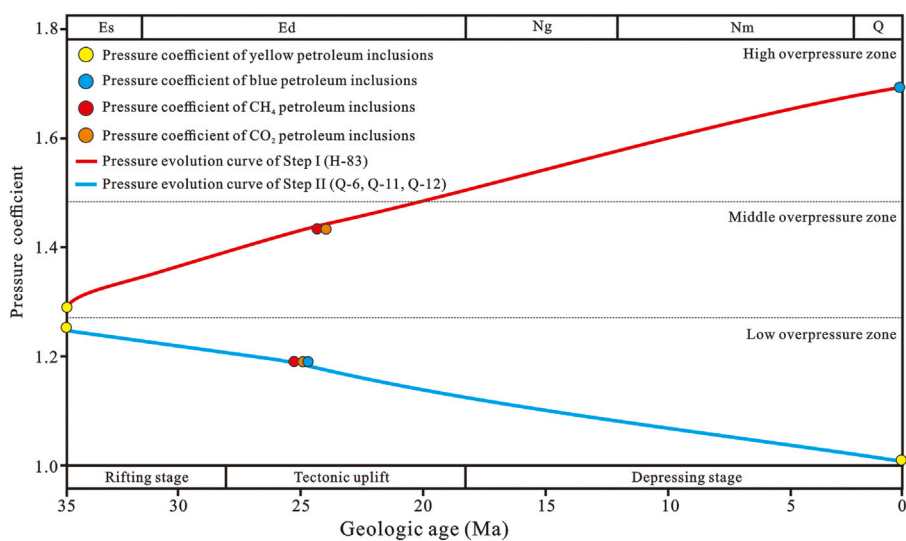


FIGURE 10

Pressure coefficient evolutionary process of fluid inclusions in the Es_3^2 Formation in different tectonic steps of the western slope belt of Dongpu Sag.

initial conditions (Parry and Bruhn, 1990; Evans, 1995). Recovering the paleo-pressure of pure CH_4 and CO_2 gas inclusions by Raman spectroscopy quantitative analysis and the minimum trapped pressure of petroleum inclusions calculated by the predictive model, we obtained the pressure evolution of the two stages of the oil charging event and one gas charging event in different tectonic units (Figure 10). In the early Oligocene, step I and step II entered the basin rifting stage, and the source rock was in the middle stage of oil generation. Saffron yellow petroleum inclusions are largely trapped in reservoir sandstone. The reservoir maintains moderate overpressure with a pressure coefficient between 1.25 and 1.28. In the middle Oligocene, and the Dongying movement resulted in severe uplift and denudation of step II. The late Oligocene–Miocene oil reservoir degraded into CH_4 and CO_2 gas reservoirs, and the reservoir pore pressure decreased (average P_c : 1.20). The wells of step I have only minor uplift denudation. With the reburial of the Es_3 Formation, step I entered late oil generation in the late Miocene, and the maturity simulation was basically the same as the maturity of the pale blue petroleum inclusions. The pore pressure of the reservoir is approximately 1.67, which is at high overpressure conditions, and step II enters the middle stage of oil generation again (R_o %: 0.5–0.7). The maturity of late crude oil is consistent with that of trapped saffron yellow petroleum inclusions. Reservoirs maintain normal pressure conditions (average P_c : 0.90).

Conclusion

In this research, multifarious paleo-fluids occurring in the sandstone reservoir of the Shahejie Formation provide information

to pursue the pressure–temperature–time–composition (P – T – t – X). According to the previously mentioned results, the following conclusions can be reached:

- 1) Based on *in situ* Raman characteristic peak observations, fluorescence spectrum analysis, and microthermometry measurements, the fluid charging sequence of fluids in two types of reservoirs with different pressure states in Dongpu Sag is determined. The combination of the T_h throwing-dot method and buried and thermal models can be used to constrain the gas or oil accumulation times. In well H-83 of step I (high overpressure reservoir), saffron yellow petroleum inclusions of low maturation accumulated in the early Oligocene (T_h interval: 110.0–130.0°C). CH_4 and CO_2 fluid accumulated at ~24–21 Ma (density of CH_4 gas inclusions: 0.1772–0.1785 g/cm³; density of CO_2 gas inclusions: 0.608–0.665 g/cm³). Late generated oil (pale blue petroleum inclusions) with high maturation accumulated at ~12–0 Ma (T_h interval: 150.0–160.0°C). In wells Q-6, Q-11, and Q-12 of step II (normal pressure reservoir), saffron yellow petroleum inclusions accumulated at ~33–30 Ma, and after the uplift and denudation of the Dongying movement, the source rocks were buried deep again. Secondary oil generation accumulated at 4–0 Ma (T_h interval: 115.0–125.0°C). Low-abundance pale blue petroleum inclusions and high-abundance CH_4 and CO_2 gas inclusions are observed, which accumulated at ~28–20 Ma (density of CH_4 gas inclusions: 0.1010–0.1339 g/cm³; density of CO_2 gas inclusions: 0.450–0.612 g/cm³).
- 2) The recovery of paleo-pressure of CO_2 and CH_4 gas inclusions by Raman quantitative analysis and the minimum trapped pressure of oil inclusions were

determined. Both types of oil reservoirs existed in the early Oligocene under medium-overpressure conditions (P_c : 1.25–1.28). In the middle Oligocene, the Dongying movement resulted in different degrees of uplift and denudation in the two types of reservoirs, causing the reservoir to change to different pressure preservation conditions. Step I involved late oil generation in the late Miocene, and the maturity simulation was basically the same as the maturity of the pale blue petroleum inclusions. The pore pressure of the reservoir is approximately 1.67, which is under high-overpressure conditions. Because of the degradation and oxidation of crude oil in the early stage of step II, the fault destroys the reservoir and produces a large amount of CO₂ and CH₄ gas inclusions (P_c : ~1.20). The oil reservoir approaches normal pressure conditions. With the reburial of the Es₃ Formation, step II entered the middle stage of oil generation again (R_o ‰: 0.5–0.7). The maturity of late crude oil is consistent with that of trapped saffron yellow petroleum inclusions. Reservoirs maintain normal pressure conditions (average P_c : 0.90).

Data availability statement

The original contributions presented in the study are included in the article/Supplementary Material; further inquiries can be directed to the corresponding author.

Author contributions

YT: conceptualization, methodology, software, investigation, and writing—original draft. YW: Data processing and chart drawing. RW: validation, formal analysis, and visualization. YH: review and editing. YX: provided core and data. ZC: Review. TX: validation, formal analysis, and review and editing. TW: review and editing. HL: review and editing. All authors reviewed the article.

References

- Azbej, T., Severs, M. J., Rusk, B. G., and Bodnar, R. J. (2007). *In situ* quantitative analysis of individual H₂O–CO₂ fluid inclusions by laser Raman spectroscopy. *Chem. Geol.* 237, 255–263. doi:10.1016/j.chemgeo.2006.06.025
- Baumgartner, M., and Bakker, R. J. (2009). Raman spectroscopy of pure H₂O and NaCl–H₂O containing synthetic fluid inclusions in quartz—A study of polarization effects. *Mineral. Pet.* 95, 1–15. doi:10.1007/s00710-008-0028-z
- Becker, S. P., Fall, A., and Bodnar, R. J. (2008). Synthetic fluid inclusions. XVII. PVTX properties of high salinity H₂O–NaCl solutions (> 30 wt% NaCl): Application to fluid inclusions that homogenize by halite disappearance from porphyry copper and other hydrothermal ore deposits. *Econ. Geol.* 103, 539–554. doi:10.2113/gsecongeo.103.3.539
- Bodnar, R. J. (1993). Revised equation and table for determining the freezing point depression of H₂O–NaCl solutions. *Geochim. Cosmochim. Acta* 57, 683–684. doi:10.1016/0016-7037(93)90378-a
- Burke, E. A. J. (2001). Raman microspectrometry of fluid inclusions. *Lithos* 55, 139–158. doi:10.1016/s0024-4937(00)00043-8
- Burruss, R. C. (1987). Diagenetic palaeotemperatures from aqueous fluid inclusions: Re-equilibration of inclusions in carbonate cements by burial heating. *Mineral. Mag.* 51, 477–481. doi:10.1180/minmag.1987.051.362.02
- Burruss, R. C. (1991). *Practical aspects of fluorescence microscopy of petroleum fluid inclusions*. Oklahoma, United States: SEPM.
- Caumon, M.-C., Robert, P., Laverret, E., Tarantola, A., Randi, A., Pironon, J., et al. (2014). Determination of methane content in NaCl–H₂O fluid inclusions by Raman spectroscopy. Calibration and application to the external part of the Central Alps (Switzerland). *Chem. Geol.* 378–379, 52–61. doi:10.1016/j.chemgeo.2014.03.016
- Caumon, M.-C., Tarantola, A., and Mosser-Ruck, R. (2015). Raman spectra of water in fluid inclusions: I. Effect of host mineral birefringence on salinity measurement. *J. Raman Spectrosc.* 46, 969–976. doi:10.1002/jrs.4708

Funding

This paper was funded by the State Key Laboratory of Organic Geochemistry (Grant No. SKLOG202016), the Open Fund of the State Key Laboratory of Oil and Gas Reservoir Geology and Exploitation (Chengdu University of Technology) (Grant No. PLC20210206), the Joint Fund for Enterprise Innovation and Development (Grant No. U20B6001), and the National Natural Science Foundation of China (detection of phenylpolycyclic aromatic hydrocarbons and its petroleum geochemical significance) (Grant No. 41972148).

Acknowledgments

We thank the editor and reviewer for their constructive comments.

Conflict of interest

TX was employed by the SINOPEC Zhongyuan Oilfield Company.

The remaining authors declare that the research was conducted in the absence of any commercial or financial relationships that could be construed as a potential conflict of interest.

Publisher's note

All claims expressed in this article are solely those of the authors and do not necessarily represent those of their affiliated organizations, or those of the publisher, the editors, and the reviewers. Any product that may be evaluated in this article, or claim that may be made by its manufacturer, is not guaranteed or endorsed by the publisher.

- Chang, Y.-J., and Huang, W.-L. (2008). Simulation of the fluorescence evolution of "live" oils from kerogens in a diamond anvil cell: Application to inclusion oils in terms of maturity and source. *Geochim. Cosmochim. Acta* 72, 3771–3787. doi:10.1016/j.gca.2008.05.041
- Diamond, L. W. (2001). Review of the systematics of CO₂-H₂O fluid inclusions. *Lithos* 55, 69–99. doi:10.1016/s0024-4937(00)00039-6
- Dickinson, G. (1953). Geological aspects of abnormal reservoir pressures in Gulf Coast Louisiana. *AAPG Bull.* 37, 410–432.
- Duan, Z., and Mao, S. (2006). A thermodynamic model for calculating methane solubility, density and gas phase composition of methane-bearing aqueous fluids from 273 to 523K and from 1 to 2000bar. *Geochim. Cosmochim. Acta* 70, 3369–3386. doi:10.1016/j.gca.2006.03.018
- Duan, Z., Möller, N., and Weare, J. H. (2003). Equations of state for the NaCl-H₂O-CH₄ system and the NaCl-H₂O-CO₂-CH₄ system: Phase equilibria and volumetric properties above 573 K. *Geochim. Cosmochim. Acta* 67, 671–680. doi:10.1016/s0016-7037(02)01226-7
- Duan, Z., and Sun, R. (2003). An improved model calculating CO₂ solubility in pure water and aqueous NaCl solutions from 273 to 533 K and from 0 to 2000 bar. *Chem. Geol.* 193, 257–271. doi:10.1016/s0009-2541(02)00263-2
- Dubessy, J., Buschaert, S., Lamb, W., Pironon, J., and Thiéry, R. (2001). Methane-bearing aqueous fluid inclusions: Raman analysis, thermodynamic modelling and application to petroleum basins. *Chem. Geol.* 173, 193–205. doi:10.1016/s0009-2541(00)00275-8
- Dubessy, J., Caumon, M. C., Rull, F., and Sharma, S. (2012). Instrumentation in Raman spectroscopy: Elementary theory and practice. *Eur. Mineral. Union Notes Mineral.* 12, 83–172.
- Dubessy, J., Poty, B., and Ramboz, C. (1989). Advances in COHNS fluid geochemistry based on micro-Raman spectrometric analysis of fluid inclusions. *Eur. J. Mineral.* 1, 517–534. doi:10.1127/ejm/1/4/0517
- Evans, M. A. (1995). Fluid inclusions in veins from the Middle Devonian shales: A record of deformation conditions and fluid evolution in the Appalachian Plateau. *Geol. Soc. Am. Bull.* 107, 327–339.
- Fabre, D., and Couty, R. (1986). Investigation on the density effects in the Raman-spectrum of methane up to 3,000 bar-application to the determination of pressure in fluid inclusions trapped in minerals. *COMPTES RENDUS Acad. Sci. Ser. II* 303, 1305–1308.
- Gao, J., He, S., Zhao, J., and Yi, J. (2017). Geothermometry and geobarometry of overpressured lower Paleozoic gas shales in the Jiaoshiba field, Central China: Insight from fluid inclusions in fracture cements. *Mar. Pet. Geol.* 83, 124–139. doi:10.1016/j.marpetgeo.2017.02.018
- Gao, Z., Fan, Y., Xuan, Q., and Zheng, G. (2020). A review of shale pore structure evolution characteristics with increasing thermal maturities. *Adv. Geo-Energy Res.* 4 (4), 247–259. doi:10.46690/ager.2020.03.03
- Gay, A., Lopez, M., Berndt, C., and Seranne, M. (2007). Geological controls on focused fluid flow associated with seafloor seeps in the Lower Congo Basin. *Mar. Geol.* 244, 68–92. doi:10.1016/j.marpetgeo.2007.06.003
- Goldstein, R. H. (2001). Fluid inclusions in sedimentary and diagenetic systems. *Lithos* 55, 159–193. doi:10.1016/s0024-4937(00)00044-x
- Goldstein, R. H. (2003). Petrographic analysis of fluid inclusions. *Fluid Incl. Anal. Interpret.* 32, 9–53.
- Goldstein, R. H. (1986). Reequilibration of fluid inclusions in low-temperature calcium-carbonate cement. *Geol.* 14, 792–795. doi:10.1130/0091-7613(1986)14<792:rofil>2.0.co;2
- Guillaume, D., Teinturier, S., Dubessy, J., and Pironon, J. (2003). Calibration of methane analysis by Raman spectroscopy in H₂O-NaCl-CH₄ fluid inclusions. *Chem. Geol.* 194, 41–49. doi:10.1016/s0009-2541(02)00270-x
- Guo, H., Wang, Z., Wang, B., Zhang, Y., Meng, H., and Sui, H. (2022). Molecular dynamics simulations of oil recovery from dolomite slit nanopores enhanced by CO₂ and N₂ injection. *Adv. Geo-Energy Res.* 6 (6), 306–313. doi:10.46690/ager.2022.04.05
- Guo, H., Ying, C., Hu, Q., Lu, W., Ou, W., and Geng, L. (2014). Quantitative Raman spectroscopic investigation of geo-fluids high-pressure phase equilibria: Part I. Accurate calibration and determination of CO₂ solubility in water from 273.15 to 573.15 K and from 10 to 120 MPa. *Fluid Phase Equilibria* 382, 70–79. doi:10.1016/j.fluid.2014.08.032
- Guo, X., He, S., Liu, K., and Zheng, L. (2011). Quantitative estimation of overpressure caused by oil generation in petroliferous basins. *Org. Geochem.* 42, 1343–1350. doi:10.1016/j.orggeochem.2011.08.017
- Haszeldine, R. S., Samson, I. M., and Cornford, C. (1984). Dating diagenesis in a petroleum basin, a new fluid inclusion method. *Nature* 307, 354–357. doi:10.1038/307354a0
- Head, I. M., Larter, S. R., Gray, N. D., Sherry, A., Adams, J. J., Aitken, C. M., et al. (2010). Hydrocarbon degradation in petroleum reservoirs. *Handb. Hydrocarb. Lipid Microbiol.* 2010, 3097–3109.
- Horsfield, B., and McLimans, R. K. (1984). Geothermometry and geochemistry of aqueous and oil-bearing fluid inclusions from Fateh Field, Dubai. *Org. Geochem.* 6, 733–740. doi:10.1016/0146-6380(84)90094-9
- Huang, Y., Tarantola, A., Wang, W., Caumon, M.-C., Pironon, J., Lu, W., et al. (2018). Charge history of CO₂ in Lishui sag, East China Sea basin: Evidence from quantitative Raman analysis of CO₂-bearing fluid inclusions. *Mar. Pet. Geol.* 98, 50–65. doi:10.1016/j.marpetgeo.2018.07.030
- Hurai, V. (2010). Fluid inclusion geobarometry: Pressure corrections for immiscible H₂O-CH₄ and H₂O-CO₂ fluids. *Chem. Geol.* 278, 201–211. doi:10.1016/j.chemgeo.2010.09.014
- Kawakami, Y., Yamamoto, J., and Kagi, H. (2003). Micro-Raman densimeter for CO₂ inclusions in mantle-derived minerals. *Appl. Spectrosc.* 57, 1333–1339. doi:10.1366/000370203322554473
- Law, B. E., and Spencer, C. W. (1998). *Memoir 70, chapter 1: Abnormal pressure in hydrocarbon environments.* Oklahoma, United States: AAPG.
- Lecumberri-Sanchez, P., Steele-MacInnis, M., and Bodnar, R. J. (2012). A numerical model to estimate trapping conditions of fluid inclusions that homogenize by halite disappearance. *Geochim. Cosmochim. Acta* 92, 14–22. doi:10.1016/j.gca.2012.05.044
- Li, H., Tang, H. M., Qin, Q. R., Zhou, J. L., Qin, Z. J., Fan, C. H., et al. (2019). Characteristics, formation periods and genetic mechanisms of tectonic fractures in the tight gas sandstones reservoir: A case study of Xujiahe Formation in YB area, Sichuan Basin, China. *J. Pet. Sci. Eng.* 178, 723–735. doi:10.1016/j.petrol.2019.04.007
- Li, H., Zhou, J. L., Mou, X. Y., Guo, H. X., Wang, X. X., An, H. Y., et al. (2022). Pore structure and fractal characteristics of the marine shale of the Longmaxi Formation in the Changing area, Southern Sichuan Basin, China. *Front. Earth Sci.* 10, 1018274. doi:10.3389/feart.2022.1018274
- Li, R. F., Chen, L. Q., Li, Y. J., and Song, N. (2010). The thermal history reconstruction and hydrocarbon accumulation period discrimination of Gaoyou depression in Subei Basin. *Earth Sci. Front.* 17, 151–159.
- Liu, D., Xiao, X., Tian, H., Min, Y., Zhou, Q., Cheng, P., et al. (2013). Sample maturation calculated using Raman spectroscopic parameters for solid organics: Methodology and geological applications. *Chin. Sci. Bull.* 58, 1285–1298. doi:10.1007/s11434-012-5535-y
- Liu, J., Liu, T., Jiang, Y., Wan, T., and Liu, R. (2019). Distribution, origin, and evolution of overpressure in the Shahejie Formation of northern Dongpu depression, Bohai Bay Basin, China. *J. Pet. Sci. Eng.* 181, 106219. doi:10.1016/j.petrol.2019.106219
- Lu, W., Chou, I.-M., Burruss, R. C., and Song, Y. (2007). A unified equation for calculating methane vapor pressures in the CH₄-H₂O system with measured Raman shifts. *Geochim. Cosmochim. Acta* 71, 3969–3978. doi:10.1016/j.gca.2007.06.004
- Luo, Y., Liu, H., Zhao, Y., Wang, Y., Zhang, J., and Lü, X. (2016). Reevaluation of the origin of overpressure in the inter-salt shale-oil reservoir in Liutun Sag, Dongpu Depression, China. *J. Pet. Sci. Eng.* 146, 1092–1100. doi:10.1016/j.petrol.2016.08.011
- Mao, S., Hu, J., Zhang, D., and Li, Y. (2013). Thermodynamic modeling of ternary CH₄-H₂O-NaCl fluid inclusions. *Chem. Geol.* 335, 128–135. doi:10.1016/j.chemgeo.2012.11.003
- McLimans, R. K. (1987). The application of fluid inclusions to migration of oil and diagenesis in petroleum reservoirs. *Appl. Geochem.* 2, 585–603. doi:10.1016/0883-2927(87)90011-4
- Munz, I. A. (2001). Petroleum inclusions in sedimentary basins: Systematics, analytical methods and applications. *Lithos* 55, 195–212. doi:10.1016/s0024-4937(00)00045-1
- Munz, I. A., Wangen, M., Girard, J.-P., Lachapagne, J.-C., and Johansen, H. (2004). Pressure-temperature-time-composition (P-T-t-X) constraints of multiple petroleum charges in the Hild field, Norwegian North Sea. *Mar. Pet. Geol.* 21, 1043–1060. doi:10.1016/j.marpetgeo.2004.05.006
- Osborne, M., and Haszeldine, S. (1993). Evidence for resetting of fluid inclusion temperatures from quartz cements in oilfields. *Mar. Pet. Geol.* 10, 271–278. doi:10.1016/0264-8172(93)90109-6
- Ou, W., Guo, H., Lu, W., Wu, X., and Chou, I.-M. (2015). A re-evaluation of the effects of temperature and NaCl concentration on quantitative Raman spectroscopic measurements of dissolved CH₄ in NaCl aqueous solutions: Application to fluid inclusion analysis. *Chem. Geol.* 417, 1–10. doi:10.1016/j.chemgeo.2015.09.018
- Parry, W. T., and Bruhn, R. L. (1990). Fluid pressure transients on seismogenic normal faults. *Tectonophysics* 179, 335–344. doi:10.1016/0040-1951(90)90299-n
- Peng, D. Y., and Robinson, D. B. (1960). A new two-constant equation of state. *Minerva Ginecol.* 12, 3069–3078.

- Ping, H., Chen, H., and Thiéry, R. (2013). Thermodynamic modeling of petroleum inclusions: Composition modeling and prediction of the trapping pressure of crude oils. *Fluid Phase Equilibria* 346, 33–44. doi:10.1016/j.fluid.2013.02.016
- Ping, H., Chen, H., Zhai, P., Junzhang, Z., and Simon, C. G. (2019). Petroleum charge history in the Baiyun depression and Panyu lower uplift in the Pearl River Mouth Basin, northern South China Sea: Constraints from integration of organic geochemical and fluid inclusion data. *Am. Assoc. Pet. Geol. Bull.* 103, 1401–1442. doi:10.1306/11151817369
- Pironon, J., and Bourdet, J. (2008). Petroleum and aqueous inclusions from deeply buried reservoirs: Experimental simulations and consequences for overpressure estimates. *Geochim. Cosmochim. Acta* 72, 4916–4928. doi:10.1016/j.gca.2008.07.019
- Pironon, J., Grimmer, J. O. W., Teinturier, S., Guillaume, D., and Dubessy, J. (2003). Dissolved methane in water: Temperature effect on Raman quantification in fluid inclusions. *J. Geochem. Explor.* 78–79, 111–115. doi:10.1016/s0375-6742(03)00136-5
- Pironon, J. (1990). Synthesis of hydrocarbon fluid inclusions at low temperature. *Am. Mineral.* 75, 226–229.
- Revesz, K., Coplen, T. B., Baedeker, M. J., Glynn, P. D., and Hult, M. (1995). Methane production and consumption monitored by stable H and C isotope ratios at a crude oil spill site, Bemidji, Minnesota. *Appl. Geochem.* 10, 505–516. doi:10.1016/0883-2927(95)00021-6
- Roedder, E. (1984). *Fluid inclusions*. Chantilly, VA: Mineralogical Society of America.
- Rosso, K. M., and Bodnar, R. J. (1995). Microthermometric and Raman spectroscopic detection limits of CO₂ in fluid inclusions and the Raman spectroscopic characterization of CO₂. *Geochim. Cosmochim. Acta* 59, 3961–3975. doi:10.1016/0016-7037(95)94441-h
- Saimd, T., and Ali, M. (2006). A comparative study of the Rare Earth Element (REE) distributions within the Lower Cretaceous dolomites and limestones of Central Tunisia. *Sedimentology* 32, 897–907. doi:10.1111/j.1365-3091.1985.tb00739.x
- Seitz, J. C., Pasteris, J. D., and Chou, I. M. (1993). Raman spectroscopic characterization of gas mixtures; I, Quantitative composition and pressure determination of CH₄, N₂ and their mixtures. *Am. J. Sci.* 293, 297–321. doi:10.2475/ajs.293.4.297
- Seitz, J. C., Pasteris, J. D., and Chou, I. M. (1996). Raman spectroscopic characterization of gas mixtures; II, Quantitative composition and pressure determination of the CO₂-CH₄ system. *Am. J. Sci.* 296, 577–600. doi:10.2475/ajs.296.6.577
- Song, F., Ye, J., and Shen, C. (2010). Hydrocarbon filling history in the western slope belt of Dongpu depression. *Nat. Gas. Geosci.* 21, 264–269.
- Thiery, R., Pironon, J., Walgenwitz, F., and Montel, F. (2000). PIT (petroleum inclusion thermodynamic): A new modeling tool for the characterization of hydrocarbon fluid inclusions from volumetric and microthermometric measurements. *J. Geochem. Explor.* 69, 701–704. doi:10.1016/s0375-6742(00)00085-6
- Tingay, M. R., Hillis, R. R., Swarbrick, R. E., Morley, C. K., and Damit, A. R. (2009). Origin of overpressure and pore-pressure prediction in the Baram province, Brunei. *Am. Assoc. Pet. Geol. Bull.* 93, 51–74. doi:10.1306/08080808016
- Van den Kerkhof, A. M., and Hein, U. F. (2001). Fluid inclusion petrography. *Lithos* 55, 27–47. doi:10.1016/s0024-4937(00)00037-2
- Wang, R., Ding, W., Zhang, Y., Wang, Z., Wang, X., He, J., et al. (2016a). Analysis of developmental characteristics and dominant factors of fractures in Lower Cambrian marine shale reservoirs: A case study of Niutitang Formation in Cen'gong block, southern China. *J. Petroleum Sci. Eng.* 138, 31–49. doi:10.1016/j.petrol.2015.12.004
- Wang, R., Gu, Y., Ding, W., Gong, D., Yin, S., Wang, X., et al. (2016b). Characteristics and dominant controlling factors of organic-rich marine shales with high thermal maturity: A case study of the Lower Cambrian Niutitang Formation in the Cen'gong block, southern China. *J. Nat. Gas Sci. Eng.* 33, 81–96. doi:10.1016/j.jngse.2016.05.009
- Wang, W., Caumon, M.-C., Tarantola, A., Pironon, J., Lu, W., and Huang, Y. (2019). Raman spectroscopic densimeter for pure CO₂ and CO₂-H₂O-NaCl fluid systems over a wide PT range up to 360° C and 50 MPa. *Chem. Geol.* 528, 119281. doi:10.1016/j.chemgeo.2019.119281
- Wang, X., Chou, I. M., Hu, W., Burruss, R. C., Sun, Q., and Song, Y. (2011). Raman spectroscopic measurements of CO₂ density: Experimental calibration with high-pressure optical cell (HPOC) and fused silica capillary capsule (FSCC) with application to fluid inclusion observations. *Geochim. Cosmochim. Acta* 75, 4080–4093. doi:10.1016/j.gca.2011.04.028
- Weibull, W., Mienert, J., Bünz, S., and Hustoft, S. (2010). Fluid migration directions inferred from gradient of time surfaces of the sub seabed. *Mar. Pet. Geol.* 27, 1898–1909. doi:10.1016/j.marpetgeo.2010.07.014
- Wilkins, R. W. T., Boudou, R., Sherwood, N., and Xiao, X. (2014). Thermal maturity evaluation from inertinites by Raman spectroscopy: The 'RaMM' technique. *Int. J. Coal Geol.* 128–129, 143–152. doi:10.1016/j.coal.2014.03.006
- Wilkins, R. W. T., Sherwood, N., and Li, Z. (2018). RaMM (Raman maturity method) study of samples used in an interlaboratory exercise on a standard test method for determination of vitrinite reflectance on dispersed organic matter in rocks. *Mar. Pet. Geol.* 91, 236–250. doi:10.1016/j.marpetgeo.2017.12.030
- Wilkins, R. W. T., Wang, M., Gan, H., and Li, Z. (2015). A RaMM study of thermal maturity of dispersed organic matter in marine source rocks. *Int. J. Coal Geol.* 150–151, 252–264. doi:10.1016/j.coal.2015.09.007
- Wu, J., and Ye, J. (2009). Fluid history analysis in the western slope belt of Dongpu Sag. *Geol. Sci. Technol. Inf.* 28, 66–70.
- Zhang, J., Qiao, S., Lu, W., Hu, Q., Chen, S., and Liu, Y. (2016). An equation for determining methane densities in fluid inclusions with Raman shifts. *J. Geochem. Explor.* 171, 20–28. doi:10.1016/j.gexplo.2015.12.003
- Zozulya, A. A., Diddams, S. A., and Clement, T. S. (1998). Investigations of nonlinear femtosecond pulse propagation with the inclusion of Raman, shock, and third-order phase effects. *Phys. Rev. A* 58, 3303–3310. doi:10.1103/physreva.58.3303
- Zuo, Y. H., Ye, B., Wu, W., Zhang, Y., Ma, W., Tang, S., et al. (2017). Present temperature field and Cenozoic thermal history in the Dongpu depression, Bohai Bay Basin, north China. *Mar. Pet. Geol.* 88, 696–711. doi:10.1016/j.marpetgeo.2017.08.037